The effect of particle density in turbulent channel flow laden with finite size particles in semi-dilute conditions

W. Fornari, A. Formenti, F. Picano, and L. Brandt

Citation: Physics of Fluids **28**, 033301 (2016); doi: 10.1063/1.4942518
View online: http://dx.doi.org/10.1063/1.4942518
View Table of Contents: http://scitation.aip.org/content/aip/journal/pof2/28/3?ver=pdfcov
Published by the AIP Publishing

PHYSICS OF FLUIDS **28**, 033301 (2016)

The effect of particle density in turbulent channel flow laden with finite size particles in semi-dilute conditions

W. Fornari,[1] A. Formenti,[2] F. Picano,[2] and L. Brandt[1]
[1]*SeRC and Linné FLOW Centre, KTH Mechanics, SE-100 44 Stockholm, Sweden*
[2]*Department of Industrial Engineering, University of Padova, Via Venezia 1, 35131 Padova, Italy*

(Received 14 October 2015; accepted 5 February 2016; published online 1 March 2016)

We study the effect of varying the mass and volume fraction of a suspension of rigid spheres dispersed in a turbulent channel flow. We performed several direct numerical simulations using an immersed boundary method for finite-size particles changing the solid to fluid density ratio R, the mass fraction χ, and the volume fraction ϕ. We find that varying the density ratio R between 1 and 10 at constant volume fraction does not alter the flow statistics as much as when varying the volume fraction ϕ at constant R and at constant mass fraction. Interestingly, the increase in overall drag found when varying the volume fraction is considerably higher than that obtained for increasing density ratios at same volume fraction. The main effect at density ratios R of the order of 10 is a strong shear-induced migration towards the centerline of the channel. When the density ratio R is further increased up to 1000, the particle dynamics decouple from that of the fluid. The solid phase behaves as a dense gas and the fluid and solid phase statistics drastically change. In this regime, the collision rate is high and dominated by the normal relative velocity among particles. © *2016 AIP Publishing LLC.* [http://dx.doi.org/10.1063/1.4942518]

I. INTRODUCTION

The transport of particles in flows is relevant to many industrial applications and environmental processes. Examples include sediment transport in rivers, avalanches and pyroclastic flows, as well as many oil industry and pharmaceutical processes. Often the flow regime encountered in such applications is turbulent due to the high flow rates and it can be substantially affected by the presence of the solid phase. Depending on the features of both fluid and solid phases, many different scenarios can be observed and the understanding of such flows is still incomplete.

The rheological properties of these suspensions have mainly been studied in the viscous Stokesian regime and in the low speed laminar regime. Even limiting our attention to monodisperse rigid neutrally buoyant spheres suspended in Newtonian liquids, we find interesting rheological behaviors such as shear thinning or thickening, jamming at high volume fractions, and the generation of high effective viscosities and normal stress differences.[1–3] It is known that the effective viscosity of a suspension μ_e changes with respect to that of the pure fluid μ due to the modification of the response of the complex fluid to the local deformation rate.[4] In the dilute regime, an expression for the effective viscosity μ_e with the solid volume fraction ϕ has first been proposed by Einstein[5,6] and then corrected by Batchelor[7] and Batchelor and Green.[8] As the volume fraction increases, the mutual interactions among particles become more important and the effective viscosity increases until the system jams.[9] At high volume fractions, the variation of the effective viscosity μ_e is described exclusively by semi-empirical laws such as those by Eiler and Krigher and Dougherty[1] that also capture the observed divergence at the maximum packing limit,[10] $\phi_m = 0.58$–0.62. In laminar flows, shear-thickening or normal stress differences occur due to inertial effects at the particle scale. Indeed, when the particle Reynolds number Re_a is non-negligible, the symmetry of the particle pair trajectories is broken and the microstructure becomes anisotropic, leading to macroscopical behaviors such as shear-thickening.[11–13] Finally, in the highly inertial regime, the effective viscosity μ_e increases linearly with shear rate due to augmented particle collisions.[14]

Another important feature observed in viscous flows is shear-induced migration. When considering a pressure-driven Poiseuille flow, either in a tube or in a channel, the particles irreversibly migrate toward the centerline, i.e., from high to low shear rate regions.[4,15] Interestingly when inertial effects become important, a different kind of migration occurs as the particles tend to move radially away from both the centerline and the walls, toward an intermediate equilibrium position. This type of migration was first observed in a tube[4,16] and was named tubular pinch. It is mechanistically unrelated to the rheological properties of the flow and results from the fluid-particle interaction within the conduit. The case of the laminar square duct flow has also been studied to identify the particle equilibrium positions.[17,18] It was found that finite-size particles migrate toward the corners or to the center of edges depending on the bulk Reynolds number. At high Reynolds numbers (but still in the laminar regime), some particles were also found in an inner region near the center of the duct.

Typically, as the Reynolds number is increased, inertial effects become important and the unladen flow undergoes a transition from laminar to turbulent conditions. The presence of the solid phase may alter this process by either increasing or reducing the critical Reynolds number above which the transition to the turbulent regime occurs. The case of a dense suspension of particles in a pipe flow has been studied experimentally[19] and numerically.[20] It has been suggested that transition depends upon the pipe to particle diameter ratios and the volume fraction. For larger particles, transition shows a non-monotonic behavior that cannot be solely explained in terms of an increase of the effective viscosity. For smaller neutrally buoyant particles instead, the critical Reynolds number increases monotonically with the solid volume fraction due to the raise in effective viscosity.

The transition in dilute suspensions of finite-size particles in plane channels has been studied by Lashgari *et al.*[21] and Loisel *et al.*[22] It has been shown that the critical Reynolds number above which turbulence is sustained is reduced. At fixed Reynolds number and solid volume fraction, the initial arrangement of particles is important to trigger the transition. Lashgari *et al.*[23] also investigated numerically a channel flow laden with solid spherical particles at higher volume fractions and for a wide range of Reynolds numbers. These authors identified three different regimes for different values of the solid volume fraction ϕ and the Reynolds number Re. In each regime (laminar, turbulent, and inertial shear-thickening), the flow is dominated by different components of the total stress (viscous, turbulent, or particle stresses, respectively).

Regarding the fully turbulent regime, most of the previous studies have focused on dilute or very dilute suspensions of particles smaller than the hydrodynamic scales and heavier than the fluid. In the one-way coupling regime[24] (i.e., when the solid phase has a negligible effect on the fluid phase) and limiting our attention to wall-bounded flows, it has been shown that particles migrate from regions of high to low turbulence intensities.[25] This phenomenon is known as turbophoresis and it has been shown to be stronger when the turbulent near-wall characteristic time and the particle inertial time scale are similar.[26] Small-scale clustering has also been observed in this kind of inhomogeneous flows,[27] leading together with turbophoresis to the formation of streaky particle patterns.[28] In the two-way coupling regime (i.e., when the mass density ratios are high and the back-reaction of the dispersed phase on the fluid cannot be neglected), the solid phase has been shown to reduce the turbulent near-wall fluctuations increasing their anisotropy[29] and eventually reducing the total drag.[30]

When the suspensions are dense, it is of fundamental importance to consider particle-particle interactions and collisions. Indeed, the chaotic dynamics of the fluid phase affects the rheological properties of the suspension, especially at high Reynolds numbers. This is known as a four-way coupling regime. Increasing the particle size directly affects the turbulent structures at smaller and comparable scales[31] thereby modulating the turbulent field. In a turbulent channel flow, it has been reported that finite-size particles larger than the dissipative length scale increase the turbulent intensities and the Reynolds stresses.[32] Particles are also found to preferentially accumulate in the near-wall low-speed streaks.[32] This has also been observed in open channel flows laden with heavy finite-size particles. In this case, the flow structures are found to have a smaller streamwise velocity.[33,34]

Concerning turbulent channel flows of neutrally buoyant particles, recent studies with $\phi \simeq 7\%$ report that due to the attenuation of the large-scale streamwise vortices, the fluid streamwise velocity fluctuation is reduced. When the particles are heavier than the carrier fluid and therefore sediment, the bottom wall acts as a rough boundary which makes the particles resuspend.[35] Recent simulations from our group have shown that the overall drag increases as the volume fraction is increased from $\phi = 0\%$ up to 20%. This trend cannot be solely explained in terms of the increase of the suspension effective viscosity. It is instead found that as particle volume fraction increases, the velocity fluctuation intensities and the Reynolds shear stresses decrease while there is a significant increase of the particle induced stresses. The latter, in turn, lead to a higher overall drag.[36]

As noted by Prosperetti,[37] however, results obtained for solid to fluid density ratios $R = \rho_p/\rho_f = 1$ cannot be easily extrapolated to other cases (e.g., when $R > 1$). In the present study, we therefore investigate numerically the effects of varying the density ratio R of the suspended phase and consequently the mass fraction χ for different volume fractions. The aim is to understand separately the effects of excluded volume and (particle and fluid) inertia on the statistical observables of both phases. To isolate the effects of different density ratios R on the macroscopical behavior of the suspension, we consider an ideal situation where the effect of gravity is neglected, leaving its analysis to future studies.

We consider a turbulent channel flow laden with rigid spheres of radius $a = h/18$, where h is the half-channel height (see Picano *et al.*[36]). Direct numerical simulations (DNS) fully describing the solid phase dynamics via an immersed boundary method (IBM) are performed as in Lucci *et al.*[38] and Kidanemariam *et al.*[33] among others. First, cases at fixed mass fractions $\chi = 0.2$ are examined and compared to cases with constant volume fraction $\phi = 5\%$ and density ratios R ranging from 1 to 10. It is observed that the influence of the density ratio R on the statistics of both phases is less important than that of an increasing volume fraction ϕ. The main effects at density ratio $R \sim 10$ are shear-induced migration towards the centerline of the channel and slight reduction of the fluid velocity fluctuations in the log-layer. The results drastically change when further increasing R (up to ~1000). It is found that for sufficiently high R ($\gtrsim$100), the solid phase behaves as a dense gas uncorrelated to the details of the carrier fluid flow.

II. METHODOLOGY

A. Numerical method

Different methods have been proposed in the last years to perform direct numerical simulations of multiphase flows. In the present study, simulations have been performed using the algorithm originally developed by Breugem[39] that fully describes the coupling between the solid and fluid phases. The Eulerian fluid phase is evolved according to the incompressible Navier-Stokes equations,

$$\nabla \cdot \mathbf{u}_f = 0, \tag{1}$$

$$\frac{\partial \mathbf{u}_f}{\partial t} + \mathbf{u}_f \cdot \nabla \mathbf{u}_f = -\frac{1}{\rho_f}\nabla p + \nu \nabla^2 \mathbf{u}_f + \mathbf{f}, \tag{2}$$

where $\mathbf{u}_f$, ρ_f, and $\nu = \mu/\rho_f$ are the fluid velocity, density, and kinematic viscosity, respectively (μ is the dynamic viscosity), while p and $\mathbf{f}$ are the pressure and a generic force field (used to model the presence of particles). The particles centroid linear and angular velocities, $\mathbf{u}_p$ and $\boldsymbol{\omega}_p$ are instead governed by the Newton-Euler Lagrangian equations,

$$\rho_p V_p \frac{d\mathbf{u}_p}{dt} = \rho_f \oint_{\partial \mathcal{V}_p} \boldsymbol{\tau} \cdot \mathbf{n}\, dS, \tag{3}$$

$$I_p \frac{d\boldsymbol{\omega}_p}{dt} = \rho_f \oint_{\partial \mathcal{V}_p} \mathbf{r} \times \boldsymbol{\tau} \cdot \mathbf{n}\, dS, \tag{4}$$

where $V_p = 4\pi a^3/3$ and $I_p = 2\rho_p V_p a^2/5$ are the particle volume and moment of inertia; $\boldsymbol{\tau} = -p\mathbf{I} + 2\mu\mathbf{E}$ is the fluid stress, with $\mathbf{E} = \left(\nabla \mathbf{u}_f + \nabla \mathbf{u}_f^T\right)/2$ the deformation tensor; $\mathbf{r}$ is the distance vector from the center of the sphere while $\mathbf{n}$ is the unity vector normal to the particle surface

$\partial\mathcal{V}_p$. Dirichlet boundary conditions for the fluid phase are enforced on the particle surfaces as $\mathbf{u}_f|_{\partial\mathcal{V}_p} = \mathbf{u}_p + \boldsymbol{\omega}_p \times \mathbf{r}$.

In the numerical code, an immersed boundary method is used to couple the fluid and solid phases. The boundary condition at the moving particle surface (i.e., $\mathbf{u}_f|_{\partial\mathcal{V}_p} = \mathbf{u}_p + \boldsymbol{\omega}_p \times \mathbf{r}$) is modeled by adding a force field on the right-hand side of the Navier-Stokes equations. The fluid phase is therefore evolved in the whole computational domain using a second order finite difference scheme on a staggered mesh while the time integration is performed by a third order Runge-Kutta scheme combined with a pressure-correction method at each sub-step. The same integration scheme is also used for the Lagrangian evolution of Eqs. (3) and (4). Each particle surface is described by uniformly distributed N_L Lagrangian points. The force exchanged by the fluid on the particles is imposed on each lth Lagrangian point and is related to the Eulerian force field $\mathbf{f}$ by the expression $\mathbf{f}(\mathbf{x}) = \sum_{l=1}^{N_L} \mathbf{F}_l \delta_d(\mathbf{x} - \mathbf{X}_l)\Delta V_l$. In the latter, ΔV_l represents the volume of the cell containing the lth Lagrangian point while δ_d is the Dirac delta. This force field is calculated through an iterative algorithm that ensures a second order global accuracy in space. In order to maintain accuracy, Eqs. (3) and (4) are rearranged in terms of the IBM force field,

$$\rho_p V_p \frac{d\mathbf{u}_p}{dt} = -\rho_f \sum_{l=1}^{N_l} \mathbf{F}_l \Delta V_l + \rho_f \frac{d}{dt} \int_{\mathcal{V}_p} \mathbf{u}_f \, dV, \tag{5}$$

$$I_p \frac{d\boldsymbol{\omega}_p}{dt} = -\rho_f \sum_{l=1}^{N_l} \mathbf{r}_l \times \mathbf{F}_l \Delta V_l + \rho_f \frac{d}{dt} \int_{\mathcal{V}_p} \mathbf{r} \times \mathbf{u}_f \, dV, \tag{6}$$

where $\mathbf{r}_l$ is the distance from the center of a particle while the second terms on the right-hand sides are corrections to account for the inertia of the fictitious fluid contained within the particle volume. Particle-particle interactions are also considered. When the gap distance between two particles is smaller than twice the mesh size, lubrication models based on Brenner's asymptotic solution[40] are used to correctly reproduce the interaction between the particles. A soft-sphere collision model is used to account for collisions between particles and between particles and walls. An almost elastic rebound is ensured with a restitution coefficient set at 0.97. These lubrication and collision forces are added to the right-hand side of Eq. (5). For more details and validations of the numerical code, the reader is referred to previous publications.[36,39,41,42]

B. Flow configuration

We consider a turbulent channel flow between two infinite flat walls located at $y = 0$ and $y = 2h$, where y is the wall-normal direction while x and z are the streamwise and spanwise directions. The domain has size $L_x = 6h$, $L_y = 2h$, and $L_z = 3h$ and periodic boundary conditions are imposed in the streamwise and spanwise directions. A fixed value of the bulk velocity U_0 is achieved by imposing a mean pressure gradient in the streamwise direction. The imposed bulk Reynolds number is equal to $Re_b = U_0 2h/\nu = 5600$ (where ν represents the kinematic viscosity of the fluid) and corresponds to a Reynolds number based on the friction velocity $Re_\tau = U_* h/\nu = 180$ for the single phase case. The friction velocity is defined as $U_* = \sqrt{\tau_w/\rho_f}$, where τ_w is the stress at the wall. A cubic staggered mesh of $864 \times 288 \times 432$ grid points is used to discretize the domain. All results will be reported either in non-dimensional outer units (scaled by U_0 and h) or in inner units (with the superscript "+," scaled by U_* and $\delta_* = \nu/U_*$).

The solid phase consists of non-Brownian rigid spheres with a radius to channel half-width ratio fixed to $a/h = 1/18$. For a volume fraction $\phi = 5\%$, this radius corresponds to about 10 plus units. In Figure 1, we display the instantaneous streamwise velocity on four orthogonal planes together with the finite-size particles dispersed in the domain. Each particle is discretized with $N_l = 746$ Lagrangian control points while their radii are 8 Eulerian grid points long. Using an Eulerian mesh consisting of 8 grid points per particle radius ($\Delta x = 1/16$) is a good compromise in terms of computational cost and accuracy. We have performed a simulation with a finer mesh (12 points per particle radius, $\Delta x = 1/24$), $R = 1$ and $\phi = 5\%$. We find indeed that the friction Reynolds number Re_τ changes by 1%, and the velocity fluctuations change locally at most by 4%.

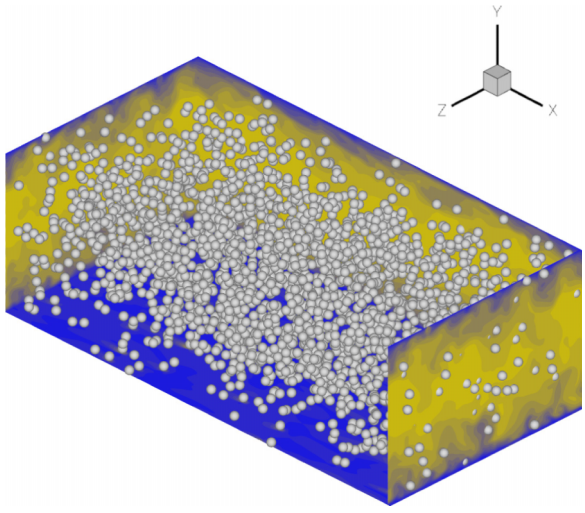

FIG. 1. Instantaneous snapshot of the streamwise velocity on different orthogonal planes together with the corresponding particle position, for $R = 10$.

At first, we will compare results obtained at different density ratios R and constant mass fraction χ with those at constant volume fraction ϕ. The mass fraction is defined as $\chi = \phi R$ and is chosen to be 0.2: four simulations are performed with $R = 1, 4, 10, 100$ and $\phi = 20\%, 5\%, 2\%, 0.2\%$ (which correspond to 10 000, 2500, 1000, and 100 particles). At constant $\phi = 5\%$ instead, we examine four cases with $R = 1, 2, 4$, and 10. The reference unladen case ($\phi = 0\%$) is also presented in the different figures. The case with $\phi = 5\%$ and $R = 1000$ will be discussed later. The full set of simulations is summarized in Table I.

The simulations start from the laminar Poiseuille flow for the fluid phase since we observe that the transition naturally occurs at the present moderately high Reynolds number, due to the noise added by the particles. Particles are initially positioned randomly with velocity equal to the local fluid velocity. Statistics are collected after the initial transient phase.

III. RESULTS

A. Analysis of mass and volume fraction effects

We show the mean fluid velocity profiles in outer and inner units ($U_f^+ = U_f/U_*$ and $y^+ = y/\delta_*$) in Figure 2. The statistics conditioned to the fluid phase have been calculated neglecting the points occupied by the solid phase in each field (phase-ensemble average). We notice in Figs. 2(a) and 2(c) that the velocity profile tends towards that for the single fluid phase as the volume fraction

TABLE I. Summary of the simulations performed (N_p is the total number of particles).

ϕ (%)	N_p	χ	R
0	0	0	...
0.2	101	0.2	100
2	1 000	0.2	10
5	2 500	0.05	1
5	2 500	0.1	2
5	2 500	0.2	4
5	2 500	0.5	10
5	2 500	50	1000
20	10 000	0.2	1

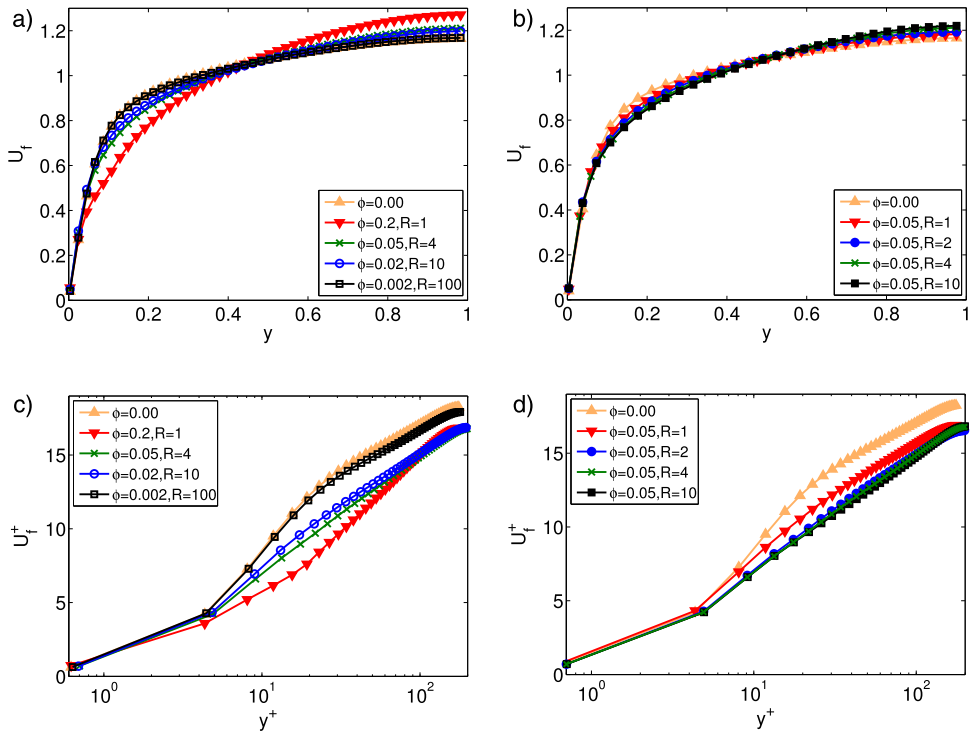

FIG. 2. Mean fluid streamwise velocity profiles for constant $\chi = 0.2$; (a) data scaled in outer units and (c) inner units. The corresponding cases at constant $\phi = 0.05$ are displayed in (b) and (d).

is reduced even if the mass fraction χ is constant. Conversely, when the volume fraction is kept constant at 5% (panels (b) and (d)) the differences observed when increasing the density ratios are small, in particular smaller velocities near the wall and larger velocities in the centre of the channel for larger χ. The decrease of the profiles in inner units, observed when increasing ϕ and less so increasing R at fixed ϕ, indicates also an overall drag increase. Indeed for $y^+ > 40$–50, the mean profile follows the log-law:[43]

$$U^+ = \frac{1}{k}\log\left(y^+\right) + B, \tag{7}$$

where k and B are the von Kármán constant and an additive coefficient. As R increases, k is found to decrease from 0.36 to 0.29 while B is reduced from 2.7 to −1.3 (see Figure 2(d)). Usually a decrease in k denotes drag reduction while a smaller or negative B leads to an increase in drag.[44] In the cases studied, this combined effect leads to a small increase of the overall drag since the friction Reynolds number Re_τ grows from 195 to 203. The reduction in the additive coefficient B is believed to be caused by the intense particle-fluid interactions occurring near the wall,[36] which are augmented by the increased inertia of the solid phase at higher R.

We report in Table II the values of k, B, and Re_τ obtained for all the cases studied. For the case with $\phi = 0.2\%$ and $R = 100$ (yet $\chi = 0.2$), we almost recover the single phase log-law with $k = 0.38$ and $B = 4.7$ (for the single fluid $k = 0.4$ and $B = 5.5$) and the increase in friction Reynolds number Re_τ is limited (from 180 to 183), which can be explained by the small number of particles in the flow. As shown above, the cases at the same mass fraction ($\chi = 0.2$) and different density ratios reveal most significant variations, explained by the changes in volume fraction ϕ (excluded volume effect).

At high ϕ, the bulk flow seems to be relaminarized, see Figure 2(a). However, although the Reynolds stresses are reduced, the particle presence induces fluctuations and enhances the overall friction via particle-induced stresses.[23,36,45]

The root-mean-square (r.m.s.) of the fluid velocity fluctuations is reported in inner units in Figure 3. Panels (a), (c), and (e) show the cases at constant χ while the cases at constant ϕ are

TABLE II. Summary of the values of the von Kármán constant k, the additive coefficient B, and the friction Reynolds number Re_τ obtained for the cases studied. The reference case with no dispersed phase is also reported. Here k and B have been fitted in the range $y^+ \in [50, 150]$.

χ	ϕ (%)	R	k	B	Re_τ
0	0	...	0.40	5.5	180
0.2	0.2	100	0.38	4.7	183
0.2	2	10	0.33	1.1	198
0.05	5	1	0.36	2.7	195
0.1	5	2	0.33	1.0	201
0.2	5	4	0.30	−0.3	202
0.5	5	10	0.29	−1.3	203
0.2	20	1	0.22	−6.3	216

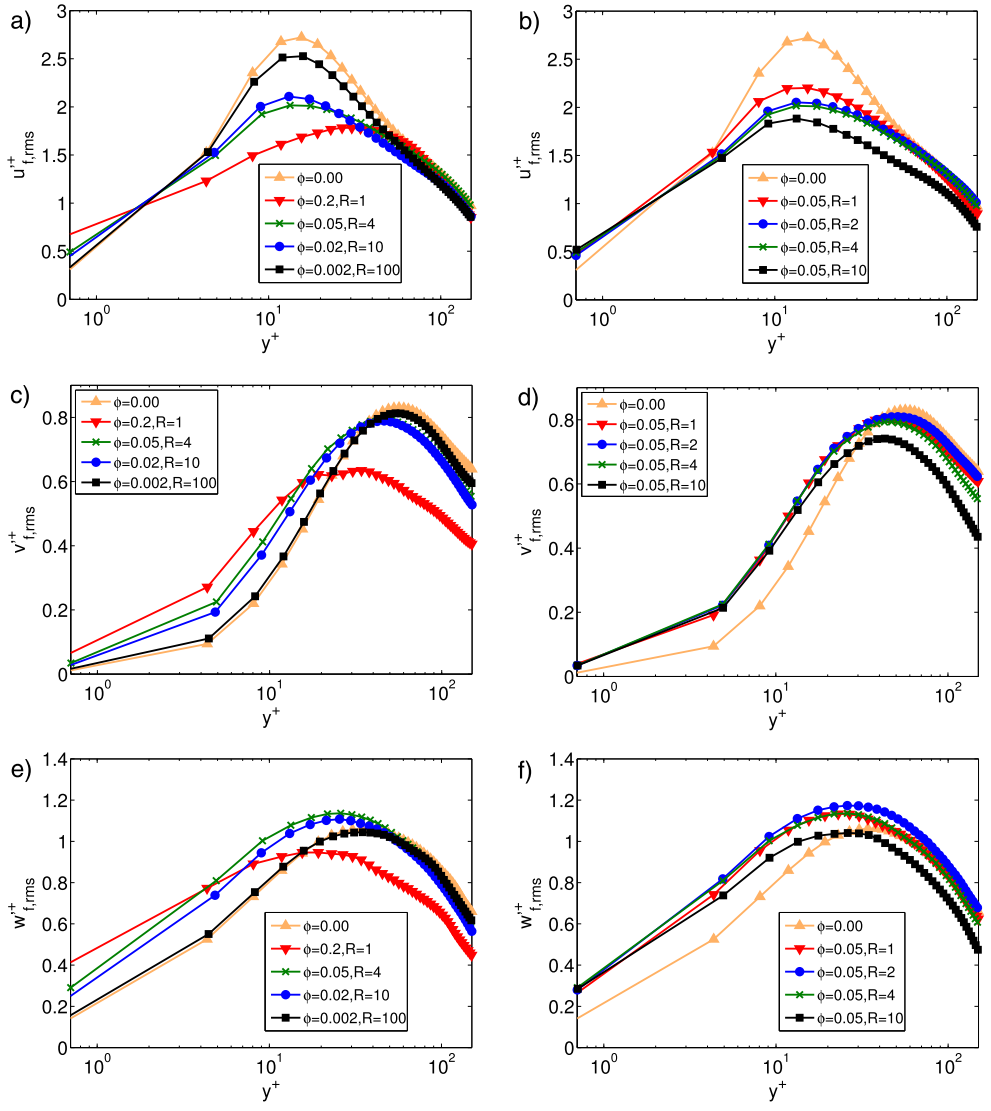

FIG. 3. Intensity of the fluctuation velocity components for the fluid phase in inner units. (a), (c), and (e) Simulations at constant mass fraction $\chi = 0.2$. (b), (d), and (f) Data at constant volume fraction $\phi = 0.05$.

reported in panels (b), (d), and (f). As for the mean flow, the major changes in fluid velocity fluctuations are associated to an increase in volume fraction ϕ. As ϕ is increased from 0.2% to 5% (constant χ), the wall-normal $v'^{+}_{f,rms}$ and spanwise components $w'^{+}_{f,rms}$ increase especially in the proximity of the wall, i.e., in the viscous sublayer. We observe also an important reduction of the streamwise fluctuation intensity around $y^+ = 10$ at higher ϕ. As we will show later, a layer of particles is formed close to the walls and the fluid between these particles and the walls is therefore squeezed. This results in a reduction of the streamwise fluid velocity fluctuations and an increase of the fluctuations in the other directions. The neutrally buoyant case at higher volume fractions ($\phi = 20\%$, $R = 1$) exhibits higher fluctuations close to the walls that drop well below the values found for the smaller volume fractions ϕ as y^+ is further increased. Only the streamwise component $u'^{+}_{f,rms}$ approaches the values obtained at smaller ϕ when $y^+ > 80$.

The fluid velocity fluctuation profiles do not show a significant dependence on the density ratio R. However, one can notice that increasing the density ratio to $R = 10$ leads to a reduction of the fluctuation intensities in all directions (when $y^+ > 5$), similarly to what observed at $R = 1$ and increasing ϕ (see previous discussion or the work by Picano and collaborators[36] for a more complete discussion). Important differences are found for $y^+ < 5$ (i.e., very close to the wall) where the velocity fluctuations increase when increasing the volume fraction while they remain approximately constant when varying R.

As mean velocity profiles are affected mostly by variations in the solid volume fraction ϕ, the explanation for the change in fluid velocity fluctuations must be searched in the context of fluid-solid interactions and of particle distribution. We therefore report in Figure 4 the local solid volume fraction along the wall-normal direction $\phi(y)$. The phase-ensemble averages for the solid phase have been obtained considering the Eulerian grid points contained within the volume of each particle at each time step. It is evident that for $R > 1$ a layer of particles forms close to the walls as soon as the volume fraction ϕ is above 0.2%.

As shown in Figure 4(b) for a constant volume fraction ($\phi = 5\%$), as the density ratio increases more particles tend to migrate toward the centerline while the layer close to the wall is preserved. The peak of $\phi(y)$ close to the wall is slightly reduced and less particles occupy the volume between $y \sim 0.1$ and 0.6. We therefore observe a shear-induced particle migration from regions of high to low shear rates, an effect more pronounced as the density ratio R increases. The local volume fraction increases drastically at the centerline ($y = 1$): the local volume fraction at the centerline $\phi(y = 1)$ is approximately twice that found at $y \sim 0.1$ (i.e., close to the wall where the first layer of particles form) when $R = 4$. The difference is even higher when $R = 10$—$\phi(y = 1) \simeq 5\phi(y = 0.1)$. This shear-induced migration becomes more intense as the density ratio R increases although, as we will see later, the picture totally changes at very high R (~1000).

We report the mean particle streamwise velocity U_p in Figure 5. The results for constant χ are shown in panel (a) where we notice that the mean particle streamwise velocity profiles are similar for $\phi = 2\%$ and 5% when $R = 10$ and 4. For $\phi = 0.2\%$ and $R = 100$ instead, the mean particle streamwise velocity profile changes drastically showing higher velocities close to the wall and smaller velocities in the rest of the channel ($y \geq 0.3$). Comparing with the other cases, we find a

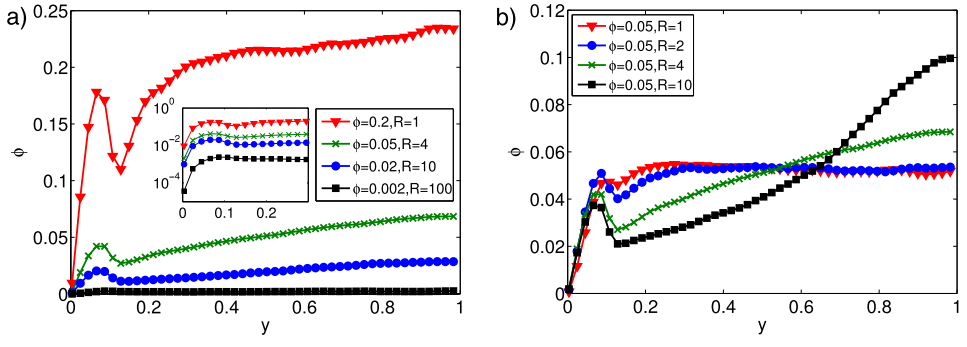

FIG. 4. Mean local volume fraction ϕ versus wall-normal coordinate y. (a) Constant $\chi = 0.2$ and (b) constant $\phi = 0.05$.

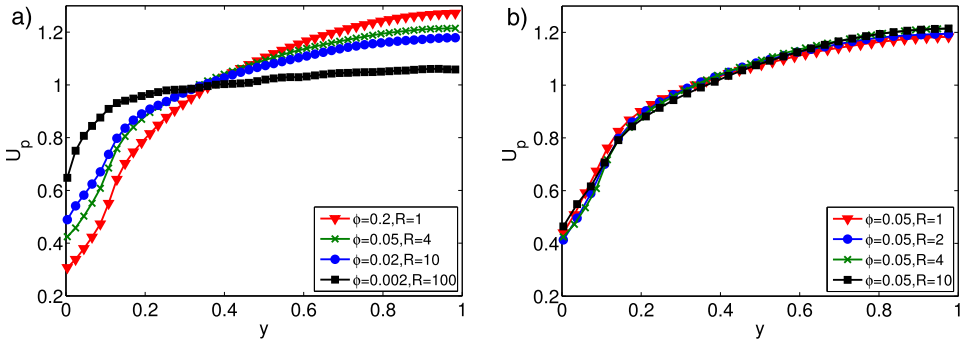

FIG. 5. Mean particle streamwise velocity profiles for (a) constant $\chi = 0.2$ and (b) constant $\phi = 0.05$.

13% reduction of U_p at the centerline. Generally we find that as the volume fraction ϕ increases, the mean particle streamwise velocity decreases closer to the walls while exhibiting higher values at the centerline.

When the volume fraction ϕ is fixed (Fig. 5(b)), U_p is only slightly altered by an increase in density ratio R. However, at the highest density ratio ($R = 10$), particles move faster in proximity of the walls and around the centerline while U_p is reduced between these two regions. The particles that lie in this region have a streamwise velocity directly linked to that of the fluid, while particles are accelerated in proximity of the wall and around the centerline where collision are more frequent. The mean particle velocity is finite close to the walls, since particles can have a relative tangential motion. The phase-ensemble averages of particle velocities are computed considering the velocities of the Eulerian grid points contained within the volume of each particle, with $\mathbf{u}(\mathbf{X},t) = \mathbf{u}_p^q(\mathbf{X}_p^q,t) + \omega_p^q(t) \times \left(\mathbf{X} - \mathbf{X}_p^q(t)\right)$ and $\mathbf{X} \in [\mathbf{X}_p^q(t) \pm a]$ (where $\mathbf{X}_p^q$ and $\mathbf{u}_p^q$ are the position of the qth particle centroid and its velocity).

In Figure 6, we show the instantaneous particle positions from the simulation with $R = 10$ projected in the streamwise-wall-normal (x–y) plane. The interaction between two approaching particles slightly shifted in the wall-normal direction and in the proximity of the wall is also sketched to explain shear-induced inertial migration. In this high shear rate region, the particle denoted by a, with velocity $U_{p,a}$, approaches particle b, moving in the same direction with velocity $U_{p,b}$. Since the latter is closer to the wall, its streamwise velocity $U_{p,b}$ is smaller (on average) than that of particle a, so a collision takes place. The scenario following this collision depends on the inertia of the fluid and solid phases, and thereby on the density ratio R.

If particles a and b are neutrally buoyant $R = 1$, their dynamics is mainly determined by the carrier fluid flow. After the collision, the two particles would tend to move radially apart and their

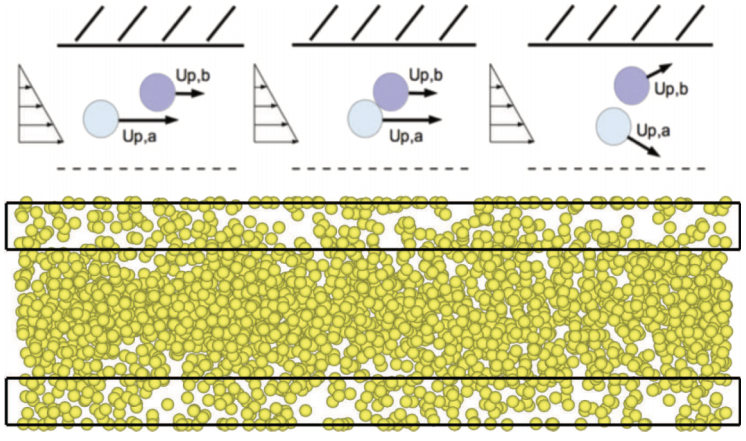

FIG. 6. Instantaneous particle positions in the x–y plane from the simulation with $R = 10$. On top, a sketch explaining the observed shear-induced migration is also presented.

motion becomes rapidly correlated to that of the fluid phase. As a result, they are on average transported downstream by the flow. As the particle inertia increases (i.e., R increases), the particle motion is less sensitive to the fluid flow and longer times are needed for the particle to adjust to the fluid velocity after the collision. Indeed, for $R \geq 4$, the particle relaxation time is longer than the fluid timescale. Therefore, particles migrate almost undisturbed in opposite wall-normal directions after a collision. Owing to the presence of the wall, we therefore observe a net migration towards the channel centre. Being this an inertial effect, the particle migration is more evident as the solid to fluid density ratio R increases. As we will discuss later, however, this effect disappears at very high density rations, R, when the particle mean velocity is almost uniform, and there is no a mean shear. On average, this inertial shear-induced migration leads to high peaks of the local solid volume fraction $\phi(y)$ at the centerline (see Figure 4(b)). The effect is so strong at $R = 10$, that it is easy to identify intermittently depleted regions of particles close to the walls (as shown in the snapshot in Figure 6).

A similar wall-normal particle migration has been observed for dense suspensions ($\phi = 30\%$) of neutrally buoyant rigid spherical particles at bulk Reynolds numbers Re_b ranging from 500 to 5000.[45] In these cases, the profiles of local volume fraction, $\phi(y)$, do not vary significantly by increasing the bulk Reynolds number and the observed migration has been attributed to the imbalance of normal stresses in the wall-normal direction. Although the resulting behavior is similar, the driving mechanisms are different.

In this section, we have studied the dependence of the suspension properties on both the solid to fluid density ratio R and the solid volume fraction ϕ. We have shown that the mean and fluctuating velocity fields of both phases are predominantly influenced by variations in the volume fraction ϕ (i.e., excluded volume effects). The mean fields are only marginally altered by increasing the density ratio R. The main effect of increasing particle inertia is the shear-induced migration just discussed.

B. Effects of density ratio *R*

In this section we discuss the results obtained in an idealized scenario where the density ratio is allowed to further increase while gravity effects are neglected. We compare results obtained at $\phi = 5\%$ and $R = 1, 10$, and 1000 showing that above a certain density ratio ($R > 10$), the solid phase decouples from the fluid leading to a completely different scenario. We have also looked at an intermediate case with density ratio $R = 100$, but being the results closer to those obtained for $R = 1000$, these have not been shown for sake of clarity.

1. Single-point statistics

The streamwise fluid velocity profiles in outer and inner units (panels (a) and (b)), the particle streamwise velocity profile (panel (c)), and the local volume fraction profile $\phi(y)$ (panel (d)) are displayed in Figure 7 for $\phi = 5\%$ and increasing particle density.

The mean fluid and particle velocity U_p changes significantly at the highest density ratio considered, $R = 1000$. The fluid velocity increases more rapidly from the wall and reaches a constant value slight above 1 for $y \gtrsim 0.3$. This value is about 12% smaller than what found at the centerline for the cases with lower density ratio. The difference between the different profiles is even more evident when the data are scaled with inner units (Fig. 7(b)). As already mentioned in Sec. III A, the mean velocity profiles are similar for density ratios between 1 and 10, still giving different coefficients for the fitting of the log-law. The velocity profiles almost overlap in the viscous sublayer and converge to approximately the same values of U_f^+ for $y^+ > 100$. For the case with $R = 1000$, instead, the mean velocity is close to that for $R = 10$ only close to the wall, $y^+ \lesssim 20$.

Larger differences are found for the solid phase velocity, Figure 7(c): the average streamwise particle velocity is constant and approximately equal to 1, the bulk value. This is similar to the behavior previously reported for $\phi = 0.2\%$ and $R = 100$. All particles move in average with the same streamwise velocity, no matter if they are close to the walls or to the centerline. Their motion seems not to be affected by turbulent fluid flow (there is a one-way coupling between phases, since

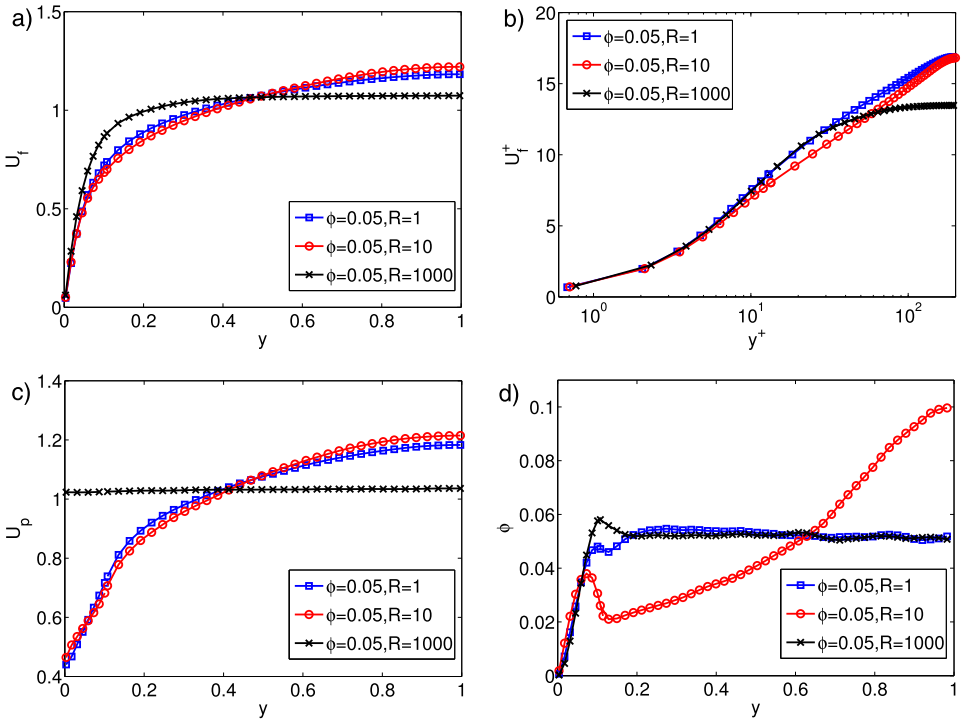

FIG. 7. Panels (a) and (b) Mean fluid streamwise velocity profiles in outer and inner units at constant $\phi = 0.05$ and increasing R. Panel (c): mean particle streamwise velocity profiles in outer units. Panel (d): mean local volume fraction ϕ versus the wall-normal coordinate y.

the fluid flow is actually modified by the presence of particles). A pseudo-plug flow is generated across the channel, as confirmed by the local volume fraction profile, $\phi(y)$, shown in Figure 7(d). Indeed, the particles are distributed almost uniformly across the channel, with the first particle layer appearing at approximately 2 particle radii from the walls.

As discussed in Sec. III A, particle inertia and near-wall shear induce particle migration toward the centerline when $R = 10$. This effect becomes more evident as the density of the particles increases, until for very high R, their inertia is so high that their motion almost completely decouples from the one of the fluid phase. In this *granular-like* regime, particles move ballistically between successive collisions and almost uniformly downstream with also an uniform wall-normal distribution. The turbulent flow structures are disrupted by these heavy particles and the typical features of a turbulent channel flow are lost.

It is now interesting to look at the particle Stokes number St_p, the ratio between the particle time scale, due to the particle inertia, and a characteristic flow time scale. We consider the convective time as flow characteristic time, $\tau_f = h/U_0 = 2h^2/(Re_b\nu)$, while the particle relaxation time is $\tau_p = \frac{4a^2R}{18\nu}$. The effect of finite inertia (i.e., of a non-negligible Reynolds number) should be taken into account in the definition of the particle Stokes number and we therefore consider the following correction of the particle drag coefficient C_D to account for inertial effects:[46]

$$C_D = \frac{24}{Re_p}\left(1 + 0.15Re_p^{0.687}\right) \tag{8}$$

(where Re_p is the particle Reynolds number) so that the modified Stokes number

$$St_p' = \frac{\tau_p}{\tau_f}\frac{1}{\left(1 + 0.15Re_p^{0.687}\right)} = \left(\frac{2a}{h}\right)^2\frac{1}{36}Re_bR\frac{1}{\left(1 + 0.15Re_p^{0.687}\right)}. \tag{9}$$

For sake of simplicity and in first approximation, we define a shear-rate based particle Reynolds number $Re_p = Re_b(a/h)^2 \sim 20$. The modified Stokes number St_p' then becomes equal to 0.9, 8.8,

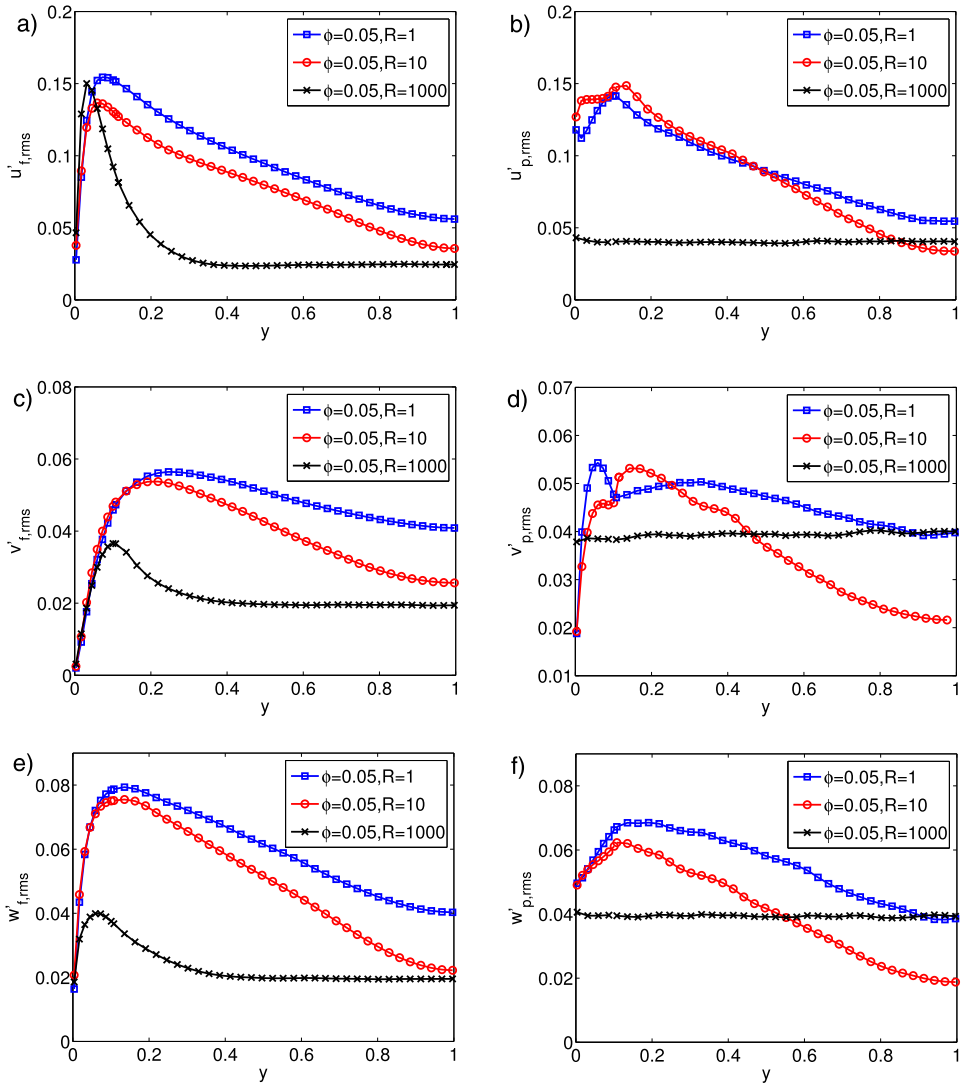

FIG. 8. Intensity of the different components of the fluctuation velocities for the fluid (panels (a), (c), and (e)) and for the solid phase (panels (b), (d), and (f)). The data are displayed in outer units at constant $\phi = 0.05$ and increasing R.

and 883 for $R = 1, 10$, and 1000. As expected, particle inertia becomes more and more relevant as the density ratio increases. For $R \in [1, 10]$ the inertia of the fluid and solid phases is comparable and they mutually influence each other. When $R = 1000$, conversely, the particle Stokes number is much larger than 1 and particles are only slightly affected by the fluid phase. The solid phase behaves as a dense gas, uncorrelated to the fluid phase.

In Figure 8, we compare the fluid and particle velocity fluctuations for the three different density ratios under investigation. It can be seen from the plots in 8(a), 8(c), and 8(e) that the fluid velocity fluctuations are significantly different at the highest R. All velocity components display larger values close to the wall and then drop rapidly to a constant value of approximately 0.02. Anisotropy in the energy distribution is maintained very close to the walls only, whereas a quasi-isotropic energy distribution is found in the rest of the channel. The particle velocity fluctuations reported in panels (b), (d), and (f) also exhibit an almost isotropic distribution, with a fluctuation intensity of about 0.04. This statistical isotropy is typical of gaseous systems and due to the strong influence of the solid phase on the fluid phase (previously explained by means of the particle Stokes number), the fluid velocity fluctuations are forced to approach a quasi-isotropic statistical steady state.

We finally observe that, approaching the centerline, particle, and fluid velocity fluctuations pertaining the case with $R = 10$ are smaller than those of the neutrally buoyant case. On average, particles are more likely to be at the channel centre and move in the direction of the pressure gradient. Fluctuations, in all directions, are therefore reduced, and due to the strong coupling between the two phases, the fluid velocity fluctuations also decrease in this more ordered structure.

2. Particle dispersion

Next, we discuss the particle dispersion in the streamwise and spanwise directions. The motion of the particles is constrained in the wall-normal direction by the presence of the walls and is therefore not examined here. The dispersion is quantified by the variance of the particle displacement as function of the separation time t. Here, we compute the mean-square displacement of the particle trajectories

$$\langle \Delta \mathbf{X}_p^2 \rangle(t) = \langle \left[\mathbf{X}_p(\bar{t} + t) - \mathbf{X}_p(\bar{t}) \right]^2 \rangle_{p,\bar{t}}, \tag{10}$$

where the square displacements are averaged over time $\bar{t}$ and the number of particles p.

Figure 9(a) shows the particle dispersion in the streamwise direction, $\langle \Delta x_p^2 \rangle$, while the spanwise dispersion, $\langle \Delta z_p^2 \rangle$, is reported in panel (b) of the same figure.

Dispersion in the streamwise direction is similar for the cases with $R = 1$ and 10. The particle trajectories are initially correlated and the displacements proportional to time t. In this so-called ballistic regime, the mean square dispersion $\langle \Delta x_p^2 \rangle$ shows a quadratic dependence on time. Only after $t \sim 100\,(2a)/U_0$, the curve approaches the linear behavior typical of a diffusive motion. This is induced by particle-particle and hydrodynamic interactions that decorrelate the trajectories in time.

As discussed above, the motion of the solid phase is almost uncorrelated to that of the fluid when increasing the density ratio to $R = 1000$. Since the mean particle velocity is flat across the channel, the dispersion is not enhanced by the inhomogeneity of the velocity profile typical of shear flows, the so-called Taylor-Aris dispersion.[47,48] Therefore $\langle \Delta x_p^2 \rangle$ is approximately one or two orders of magnitude lower than in the two cases at lower R. Interestingly, the purely diffusive behavior is attained faster and the transition from the ballistic behavior begins already at $t \approx 20\,(2a)/U_0$.

The dispersion in the spanwise direction, $\langle \Delta z_p^2 \rangle$, is similar for all density ratios R considered. Again, one can identify a quadratic and linear behavior in time with a transition between the two regimes at $t \sim 20\,(2a)/U_0$. We also note that for $t \lesssim 10\,(2a)/U_0$, the spanwise dispersion of the particles of highest density is close to that of particles with $R = 10$, while for $t \gtrsim 200\,(2a)/U_0$, the behavior appears similar to that found for $R = 1$.

To conclude this section, we emphasize that the statistics of particle dispersion reveal that the particle motion only slightly changes when increasing the particle density ratio from $R = 1$ to $R = 10$, supporting the observation that the bulk flow behavior depends more on the excluded volume, i.e., ϕ, rather than on the particle inertia.

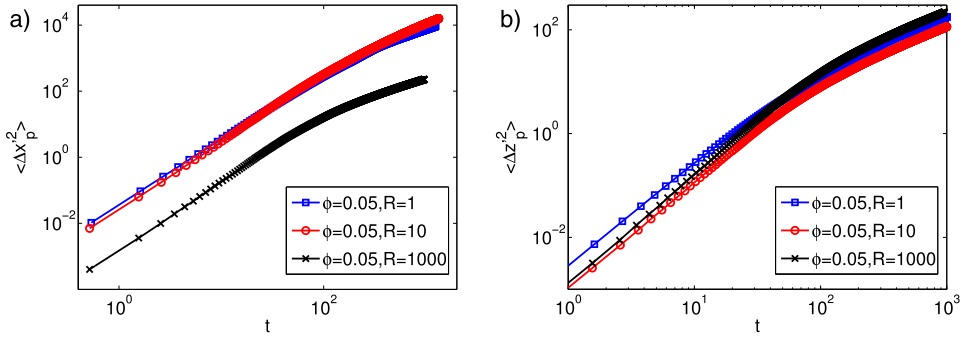

FIG. 9. Particle dispersion. Time evolution of the mean square displacement along particle trajectories from the simulations at constant $\phi = 0.05$ and increasing R. (a) Streamwise and (b) spanwise component of the dispersion.

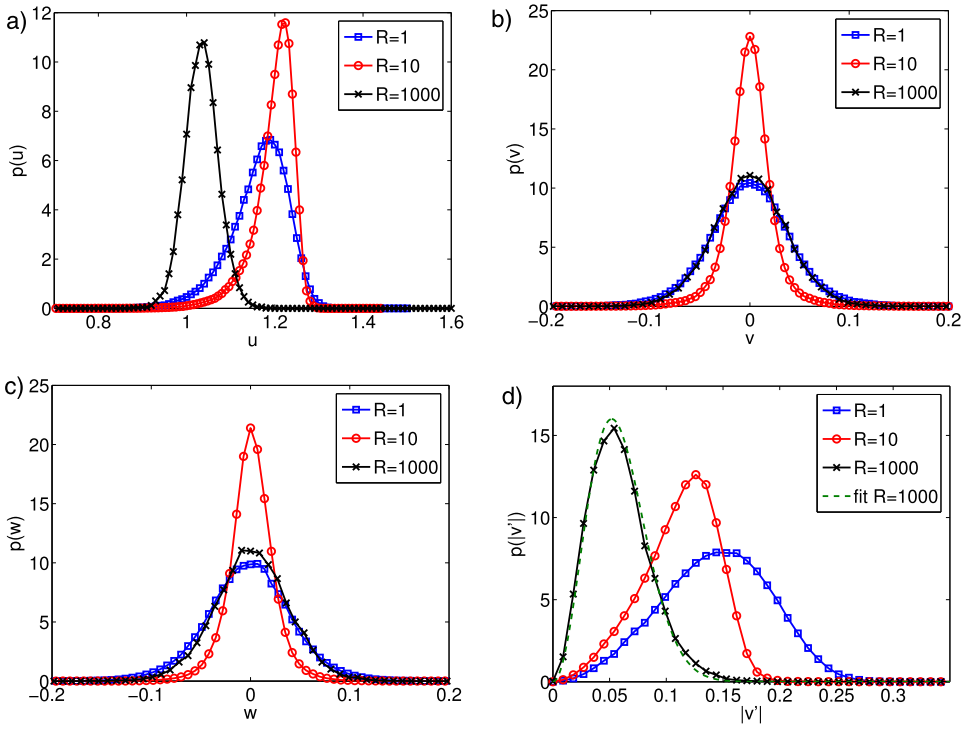

FIG. 10. Probability density function of the particle velocity around the center of the channel, for the different density ratios under investigation (panels (a)–(c) for the streamwise, wall-normal, and spanwise components, respectively). Panel (d) reports the probability density function of the magnitude of the particle velocity fluctuations around the center of the channel where a Maxwell-Boltzmann distribution is used to fit the case with $R = 1000$.

3. Particle velocity probability density functions and collision rates

We wish to give further insight on the behavior of the solid phase dynamics by examining the velocity probability density functions. We will focus on the case with $R = 1, 10$, and 1000 and calculate the probability density function $p(\cdot)$ for each component of the particle velocity in the volume around the centerline of the channel (of size $2h \times 2h/3 \times 3h$). The distributions of the streamwise, wall-normal, and spanwise components of the particle velocity are depicted in panels (a)–(c) of Figure 10.

We see in panel (a) that the distribution pertaining the streamwise component, $p(u)$, exhibits a negative skewness S (=−0.77 and −1.54) for $R = 1$ and 10, indicating that particles exhibit with higher probability intense fluctuations lower than the mean value, as observed also in single-phase turbulent channel flow.[49] As R is increased from 1 to 10, the variance σ^2 is however reduced, whereas the flatness F increases (from 3.8 to 6.9) indicating that rare events become more frequent. The results for $R = 1000$ show that the velocity distribution changes to what, at first sight, may seem a normal distribution with smaller modal value and variance, almost vanishing skewness ($S \sim 0.03$) and flatness close to 3 ($F \sim 3.3$).

The velocity distributions in the cross-stream directions (reported in panels (b) and (c)) resemble a normal distribution centered around a zero mean value. As for the streamwise component, the flatness F exhibits high values (between 6 and 7) only for $R = 10$ while for the remaining two cases, it is just slightly greater than 3.

Next, we report the probability distributions of the modulus of the velocity fluctuations,

$$|v'| = \sqrt{u'^2_{p,rms} + v'^2_{p,rms} + w'^2_{p,rms}}, \tag{11}$$

calculated in the same volume around the centerline in Figure 10(d). The most peculiar distribution is the one found for $R = 1000$. It closely resembles a Maxwell-Boltzmann distribution (or a χ

distribution with three degrees of freedom) defined as follows:

$$p(x) = \sqrt{\frac{2}{\pi}} \frac{x^2 e^{-x^2/(2a^2)}}{a^3}, \tag{12}$$

where a is a scale parameter (velocity). This distribution describes the velocity of atoms of an ideal gas that freely move inside a stationary container. In such case the scale parameter becomes $a = \sqrt{kT/m}$, where k is the Boltzmann's constant, T the thermodynamic temperature, and m the particle mass. Fitting our results with Equation (12), we find $a \sim 0.037$, corresponding to the Maxwell-Boltzmann distribution displayed in panel (d) with dashed line. The root mean square of such a distribution is $\sigma = \sqrt{3}a = 0.064$, using the value of a previously reported. Examining again Figures 8(b), 8(d), and 8(f), we notice that the velocity fluctuations are approximately equal to 0.04, with modulus $|v'| \simeq 0.069$. Thus the root mean square σ is completely defined by $|v'|$. These findings further confirm our previous speculations about the appearance of a dense gaseous regime at high density ratios R.

Finally we examine particle-pair statistics, function of the distance between the centers r, and show that the large variations of the particle velocity also affect the particle-pair dynamics, in particular the collisions. As the distance r approaches the particle diameter, the near field interactions become important and collisions may occur (whenever $r = 2a$). An indicator of the radial separation among pair of particles is the Radial Distribution Function (*RDF*). In a reference frame with origin at the centre of a particle, the *RDF* is the average number of particle centers located in the shell of radius r and thickness Δr, normalized with the number of particles of a random distribution. Formally the *RDF* is defined as

$$RDF(r) = \frac{1}{4\pi} \frac{dN_r}{dr} \frac{1}{r^2 n_0}, \tag{13}$$

where N_r is the number of particle pairs on a sphere of radius r, $n_0 = N_p(N_p - 1)/(2V)$ is the density of particle pairs in the volume V, with N_p the total number of particles. The value of the *RDF* at distances of the order of the particle radius reveals the intensity of clustering; the RDF tends to 1 as $r \to \infty$, corresponding to a random (Poissonian) distribution.

Here, we are mainly interested in the particle-pair statistics around the centerline and therefore compute the *RDF* in the volume defined by $y \in [0.67, 1.33]$ for the three density ratios $R = 1, 10$, and 1000 and volume fraction $\phi = 5\%$. The data obtained are shown in Figure 11(a). At lower density ratios, $R = 1$ and 10, the peaks of the *RDF*'s are found at exactly 2 particle radii from the centre of the reference particles. The *RDF* drops quickly to the value of the uniform distribution (i.e., 1) at $r \sim 2.25a$ in the neutrally buoyant case, whereas the decay is somewhat slower for $R = 10$, reaching the final plateau at $r \sim 3$. This difference can be explained by the shear-induced migration previously discussed: this enhances the number of particles around the centerline, thus increasing the local volume fraction and consequently the small scale clustering. At the highest density ratio under investigation, instead, the gaseous behavior of the solid phase leads to an uncorrelated statistical distribution of particles, corresponding to a constant value of the *RDF* equal to 1.

Figures 11(b) and 11(c) show the averaged normal relative velocity between two approaching particles $\langle dv_n^-(r)\rangle$, and the collision kernel $\kappa(r)$. This collision kernel[50] is obtained as the product of the $RDF(r)$ and $\langle dv_n^-(r)\rangle$,

$$\kappa(r) = RDF(r) \cdot |\langle dv_n^-(r)\rangle|, \tag{14}$$

when $r = 2a$. In the figure, we display the behavior of this observable with the distance r, which can be interpreted as the approach rate of particle pairs at distance r. The normal relative velocity of a particle pair is obtained as the projection of the relative velocity in the direction of the distance between the two interacting particles

$$dv_n(r_{ij}) = (\mathbf{u}_i - \mathbf{u}_j) \cdot \frac{(\mathbf{r}_i - \mathbf{r}_j)}{|(\mathbf{r}_i - \mathbf{r}_j)|} = (\mathbf{u}_i - \mathbf{u}_j) \cdot \frac{\mathbf{r}_{ij}}{|\mathbf{r}_{ij}|} \tag{15}$$

(where i and j denote the two particles). This scalar quantity can be either positive (when two particles depart form each other) or negative (when they approach). Hence, the averaged normal relative

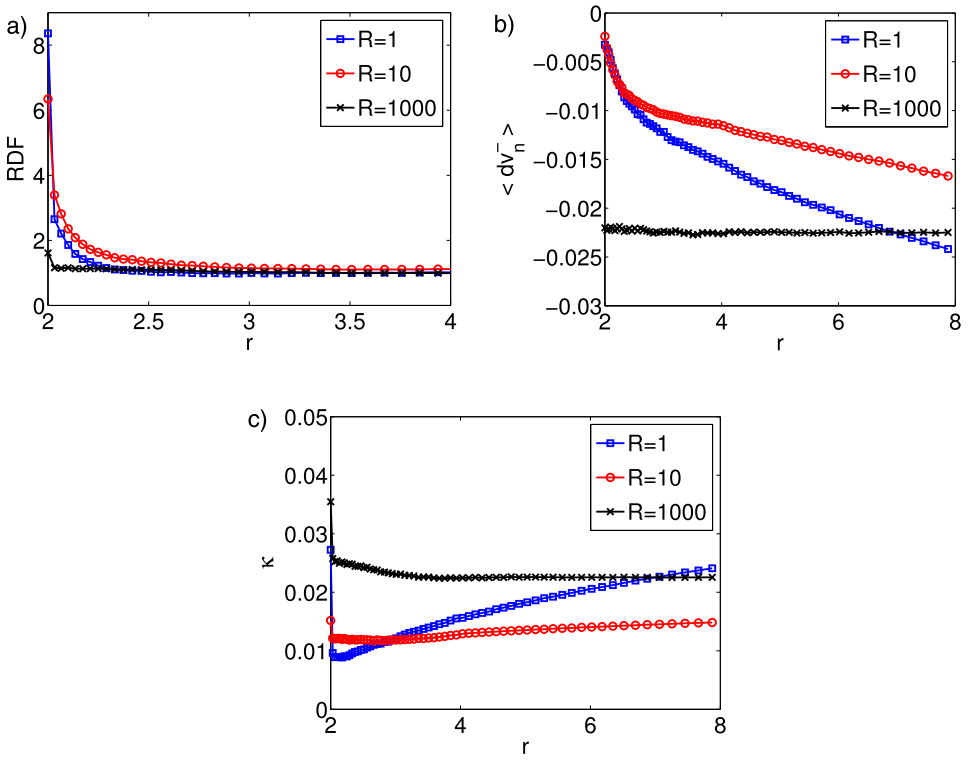

FIG. 11. (a) Radial distribution function, (b) average negative relative velocity, and (c) collision kernel (see text for the definitions) around the centerline for the three values of the density ratio R indicated and particle volume fraction $\phi = 5\%$. Distances are normalized by the particle radius.

velocity can be decomposed into $\langle dv_n(r)\rangle = \langle dv_n^+(r)\rangle + \langle dv_n^-(r)\rangle$. To estimate the probability of a collision, i.e., the collision kernel $\kappa(r)$, the mean negative normal relative velocity is therefore needed.

It is shown in Figure 11(b) that the absolute value of $\langle dv_n^-(r)\rangle$ increases with r when $R \leq 10$. Particle pairs are more likely to approach with higher speeds when further away. This increase of $|\langle dv_n^-(r)\rangle|$ with r is less pronounced for $R = 10$, which can be explained recalling that, in this case, there is a significant accumulation in the region around the centerline where the particles are transported downstream at almost constant velocity. When $R = 1000$, $|\langle dv_n^-(r)\rangle|$ is constant and equal to 0.022. In a dense gaseous regime, particles are, on average, uniformly distributed and approach each other at similar speeds and at different radial locations: their motion is uncorrelated.

The collision rate is mainly determined by the averaged normal relative velocity when $R = 1000$. As shown in Figure 11(c), $\kappa(r)$ is approximately constant at different radial distances, showing slightly larger values near contact, $r = 2a$. In the cases with $R = 1$ and 10, $\kappa(r)$ is determined at small separations r by the particle clustering and by the normal relative velocities at higher separations. When shear-induced migration occurs, $R = 10$, the collision kernel $\kappa(r)$ is higher than in the case of neutrally buoyant particles for separations between 2 and 3 particle radii. When $r \gtrsim 3$ the radial distribution function drops to 1 and the approach rate is therefore determined by the averaged normal relative velocity. Since the absolute value of $|\langle dv_n^-(r)\rangle|$ grows more slowly with r for $R = 10$, $\kappa(r)$ shows the same trend.

Before concluding the section, we examine the collision statistics when increasing the volume fraction ϕ while keeping the mass fraction χ constant. To this aim, we show in Figure 12 the radial distribution function RDF, the averaged normal relative velocity and the collision kernel from 3 of the cases at constant mass fraction previously discussed: $\phi = 2\%$ and $R = 10$; $\phi = 5\%$ and $R = 4$; $\phi = 20\%$ and $R = 1$.

The small-scale clustering increases as the volume fraction ϕ increases, see Figure 12(a), i.e., the RDF at $r = 2$ is highest for the flow with $\phi = 20\%$. However, as the excluded volume increases

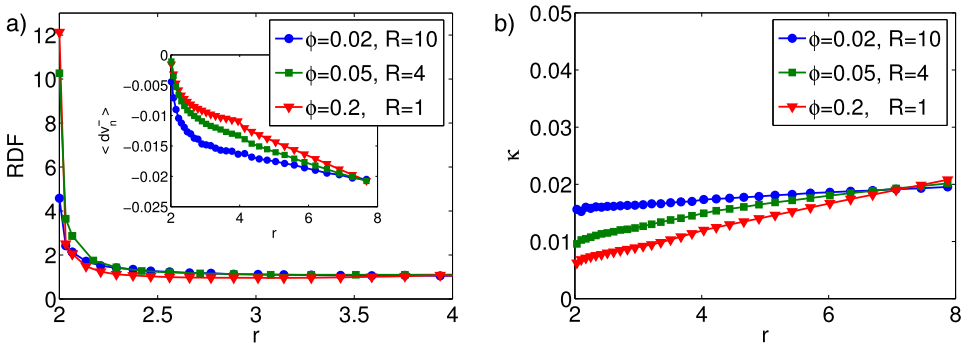

FIG. 12. (a) Radial distribution function and average negative relative velocity (inset) and (b) collision kernel (see text for the definitions) around the centerline for the three values of the density ratio R and particle volume fraction ϕ.

with ϕ, the mean distance between the particles is reduced and these approach each other on average with a smaller relative velocity, as shown by the reduction in $\langle dv_n^-(r)\rangle$ at higher ϕ in the inset of Figure 12(a). Finally, Figure 12(b) reveals that also at constant χ the collision rate is mainly governed by the averaged normal relative velocity. We observe indeed that $\kappa(r)$ is higher in the most dilute cases and the data scale with the volume fraction.

IV. FINAL REMARKS

We study the effect of varying solid to fluid density ratio and volume fraction in a turbulent channel flow laden with finite-size rigid spheres in the semi-dilute regime. The numerical simulations do not include the effect of gravity to disentangle the role of fluid and particle inertia, as well as of the excluded volume on the mean and fluctuating fluid velocities and particle motion.

The main finding of the work is that variations of the volume fraction have a larger impact on the statistics of fluid and solid phases than modifications of the density ratio R. Indeed, we show that when the volume fraction is kept constant ($\phi = 5\%$) and the density ratio, R, increased from 1 to $R \leq 10$, the mean fluid velocity and velocity fluctuation profiles are only slightly affected. The main effect of increasing the density ratio (up to $R = 10$) is the change of the mean local volume fraction, i.e., the wall-normal particle distribution across the channel. At $R = 10$, we report a significant shear-induced migration toward the centerline. This is shown to be an inertial effect induced by the particle density, R, and the presence of a wall.

When the volume fraction is changed and either the mass fraction or the density ratio kept constant, instead, the flow statistics vary significantly. The mean streamwise velocity profiles in outer units show lower values closer to the walls and higher values toward the centerline. In inner units, the difference is even more evident, showing a continuous variation of the von Kármán constant and of the additive coefficient of the log-law, see also Ref. 36 for comparisons at constant $R = 1$. The increase in overall drag found when varying the volume fraction is considerably higher than that obtained for increasing density ratios at same volume fraction.

We also consider cases at same $\phi = 5\%$ and $R = 1000$. At this high R, the motion of the solid phase decouples from the dynamics of the fluid phase and the statistics drastically change. The particles are uniformly distributed across the channel and behave as a dense gas with uniform mean streamwise velocity and uniform isotropic velocity fluctuations across the channel. The dense gas behavior of the solid phase clearly emerges in the probability density function of the modulus of the velocity fluctuations that closely follows a Maxwell-Boltzmann distribution. The fluid velocity fluctuations are reduced and are almost constant except in the regions close to the walls. For $R = 1000$, we also find that the streamwise dispersion is one or two orders of magnitude smaller than in the cases at lower R. In channel flows, the streamwise particle dispersion is enhanced by the inhomogeneity of the mean velocity profile. However as we have shown, at very high density ratios, this inhomogeneity is lost leading to a reduction of the mean streamwise particle displacement.

Finally, we have examined the radial distribution of particles and their collision kernel. For $1 \leq R \leq 10$ and constant $\phi = 5\%$, the collision rate is mostly controlled by the particle clustering near contact. Instead, for $R = 1000$, the number of collisions is enhanced and essentially determined by the particle average normal relative velocity. For suspensions at fixed mass fraction $\chi = 0.2$, the collision rate decreases with increasing ϕ.

Our results therefore suggest that the particle motion in the absence of gravity is not significantly different between neutrally buoyant particles and heavy particles with density ratios typical of sediments and metal particles in liquids. The main effects on the flow statistics are due to variations of the volume fraction, thus of the excluded volume. The main effect of increasing the density ratio is the appearance of a shear-induced migration while velocity statistics are almost unchanged. The present results may help to interpret the dynamics of sediments in shear turbulence.

ACKNOWLEDGMENTS

This work was supported by the European Research Council Grant No. ERC-2013-CoG-616186, TRITOS, from the Swedish Research Council (VR), through the Outstanding Young Researcher Award, and from the COST Action No. MP1305: *Flowing matter*. Computer time provided by SNIC (Swedish National Infrastructure for Computing) and CINECA, Italy (ISCRA Grant No. FIShnET-HP10CQQF77).

[1] J. J. Stickel and R. L. Powell, "Fluid mechanics and rheology of dense suspensions," Annu. Rev. Fluid Mech. **37**, 129–149 (2005).
[2] J. F. Morris, "A review of microstructure in concentrated suspensions and its implications for rheology and bulk flow," Rheol. Acta **48**, 909–923 (2009).
[3] N. J. Wagner and J. F. Brady, "Shear thickening in colloidal dispersions," Phys. Today **62**(10), 27–32 (2009).
[4] E. Guazzelli and J. F. Morris, *A Physical Introduction to Suspension Dynamics* (Cambridge University Press, 2011), Vol. 45.
[5] A. Einstein, "Eine neue bestimmung der moleküldimensionen," Ann. Phys. **324**, 289–306 (1906).
[6] A. Einstein, "Berichtigung zu meiner arbeit: Eine neue bestimmung der moleküldimensionen," Ann. Phys. **339**, 591–592 (1911).
[7] G. K. Batchelor, "The stress system in a suspension of force-free particles," J. Fluid Mech. **41**, 545–570 (1970).
[8] G. K. Batchelor and J. T. Green, "The determination of the bulk stress in a suspension of spherical particles to order c^2," J. Fluid Mech. **56**, 401–427 (1972).
[9] A. Sierou and J. F. Brady, "Rheology and microstructure in concentrated noncolloidal suspensions," J. Rheol. **46**, 1031–1056 (2002).
[10] F. Boyer, É. Guazzelli, and O. Pouliquen, "Unifying suspension and granular rheology," Phys. Rev. Lett. **107**, 188301 (2011).
[11] P. M. Kulkarni and J. F. Morris, "Suspension properties at finite Reynolds number from simulated shear flow," Phys. Fluids **20**, 040602 (2008).
[12] F. Picano, W.-P. Breugem, D. Mitra, and L. Brandt, "Shear thickening in non-Brownian suspensions: An excluded volume effect," Phys. Rev. Lett. **111**, 098302 (2013).
[13] J. F. Morris and H. Haddadi, "Microstructure and rheology of finite inertia neutrally buoyant suspensions," J. Fluid Mech. **749**, 431–459 (2014).
[14] R. A. Bagnold, "Experiments on a gravity-free dispersion of large solid spheres in a Newtonian fluid under shear," in *Proceedings of the Royal Society of London A: Mathematical, Physical and Engineering Sciences* (The Royal Society, 1954), Vol. 225, pp. 49–63.
[15] C. J. Koh, P. Hookham, and L. G. Leal, "An experimental investigation of concentrated suspension flows in a rectangular channel," J. Fluid Mech. **266**, 1–32 (1994).
[16] G. Segre and A. Silberberg, "Behaviour of macroscopic rigid spheres in poiseuille flow. II. Experimental results and interpretation," J. Fluid Mech. **14**, 136–157 (1962).
[17] B. Chun and A. J. C. Ladd, "Inertial migration of neutrally buoyant particles in a square duct: An investigation of multiple equilibrium positions," Phys. Fluids **18**, 031704 (2006).
[18] M. Abbas, P. Magaud, Y. Gao, and S. Geoffroy, "Migration of finite sized particles in a laminar square channel flow from low to high Reynolds numbers," Phys. Fluids **26**, 123301 (2014).
[19] J.-P. Matas, J. F. Morris, and E. Guazzelli, "Transition to turbulence in particulate pipe flow," Phys. Rev. Lett. **90**, 014501 (2003).
[20] Z. Yu, T. Wu, X. Shao, and J. Lin, "Numerical studies of the effects of large neutrally buoyant particles on the flow instability and transition to turbulence in pipe flow," Phys. Fluids **25**, 043305 (2013).
[21] I. Lashgari, F. Picano, and L. Brandt, "Transition and self-sustained turbulence in dilute suspensions of finite-size particles," Theor. Appl. Mech. Lett. **5**, 121–125 (2015).
[22] V. Loisel, M. Abbas, O. Masbernat, and E. Climent, "The effect of neutrally buoyant finite-size particles on channel flows in the laminar-turbulent transition regime," Phys. Fluids **25**, 123304 (2013).
[23] I. Lashgari, F. Picano, W.-P. Breugem, and L. Brandt, "Laminar, turbulent, and inertial shear-thickening regimes in channel flow of neutrally buoyant particle suspensions," Phys. Rev. Lett. **113**, 254502 (2014).

[24] S. Balachandar and J. K. Eaton, "Turbulent dispersed multiphase flow," Annu. Rev. Fluid Mech. **42**, 111–133 (2010).
[25] M. W. Reeks, "The transport of discrete particles in inhomogeneous turbulence," J. Aerosol Sci. **14**, 729–739 (1983).
[26] A. Soldati and C. Marchioli, "Physics and modelling of turbulent particle deposition and entrainment: Review of a systematic study," Int. J. Multiphase Flow **35**, 827–839 (2009).
[27] G. Sardina, P. Schlatter, L. Brandt, F. Picano, and C. M. Casciola, "Wall accumulation and spatial localization in particle-laden wall flows," J. Fluid Mech. **699**, 50–78 (2012).
[28] G. Sardina, F. Picano, P. Schlatter, L. Brandt, and C. M. Casciola, "Large scale accumulation patterns of inertial particles in wall-bounded turbulent flow," Flow, Turbul. Combust. **86**, 519–532 (2011).
[29] J. D. Kulick, J. R. Fessler, and J. K. Eaton, "Particle response and turbulence modification in fully developed channel flow," J. Fluid Mech. **277**, 109–134 (1994).
[30] L. H. Zhao, H. I. Andersson, and J. J. J. Gillissen, "Turbulence modulation and drag reduction by spherical particles," Phys. Fluids **22**, 081702 (2010).
[31] A. Naso and A. Prosperetti, "The interaction between a solid particle and a turbulent flow," New J. Phys. **12**, 033040 (2010).
[32] Y. Pan and S. Banerjee, "Numerical simulation of particle interactions with wall turbulence," Phys. Fluids **8**, 2733–2755 (1996).
[33] A. G. Kidanemariam, C. Chan-Braun, T. Doychev, and M. Uhlmann, "Direct numerical simulation of horizontal open channel flow with finite-size, heavy particles at low solid volume fraction," New J. Phys. **15**, 025031 (2013).
[34] A. G. Kidanemariam and M. Uhlmann, "Direct numerical simulation of pattern formation in subaqueous sediment," J. Fluid Mech. **750**, R2 (2014).
[35] X. Shao, T. Wu, and Z. Yu, "Fully resolved numerical simulation of particle-laden turbulent flow in a horizontal channel at a low Reynolds number," J. Fluid Mech. **693**, 319–344 (2012).
[36] F. Picano, W.-P. Breugem, and L. Brandt, "Turbulent channel flow of dense suspensions of neutrally buoyant spheres," J. Fluid Mech. **764**, 463–487 (2015).
[37] A. Prosperetti, "Life and death by boundary conditions," J. Fluid Mech. **768**, 1–4 (2015).
[38] F. Lucci, A. Ferrante, and S. Elghobashi, "Modulation of isotropic turbulence by particles of Taylor length-scale size," J. Fluid Mech. **650**, 5–55 (2010).
[39] W.-P. Breugem, "A second-order accurate immersed boundary method for fully resolved simulations of particle-laden flows," J. Comput. Phys. **231**, 4469–4498 (2012).
[40] H. Brenner, "The slow motion of a sphere through a viscous fluid towards a plane surface," Chem. Eng. Sci. **16**, 242–251 (1961).
[41] R. A. Lambert, F. Picano, W.-P. Breugem, and L. Brandt, "Active suspensions in thin films: Nutrient uptake and swimmer motion," J. Fluid Mech. **733**, 528–557 (2013).
[42] W. Fornari, F. Picano, and L. Brandt, "Sedimentation of finite-size spheres in quiescent and turbulent environments," J. Fluid Mech. **788**, 640–669 (2016).
[43] S. B. Pope, *Turbulent Flows* (Cambridge University Press, 2000).
[44] P. S. Virk, "Drag reduction fundamentals," AIChE J. **21**, 625–656 (1975).
[45] I. Lashgari, F. Picano, W. P. Breugem, and L. Brandt, "Channel flow of rigid sphere suspensions: Particle dynamics in the inertial regime," Int. J. Multiphase Flow **78**, 12–24 (2016).
[46] L. Schiller and A. Naumann, "A drag coefficient correlation," Vdi Zeitung **77**, 51 (1935).
[47] G. Taylor, "Dispersion of soluble matter in solvent flowing slowly through a tube," in *Proceedings of the Royal Society of London A: Mathematical, Physical and Engineering Sciences* (The Royal Society, 1953), Vol. 219, pp. 186–203.
[48] R. Aris, "On the dispersion of a solute in a fluid flowing through a tube," in *Proceedings of the Royal Society of London A: Mathematical, Physical and Engineering Sciences* (The Royal Society, 1956), Vol. 235, pp. 67–77.
[49] J. Kim, P. Moin, and R. Moser, "Turbulence statistics in fully developed channel flow at low Reynolds number," J. Fluid Mech. **177**, 133–166 (1987).
[50] S. Sundaram and L. R. Collins, "Collision statistics in an isotropic particle-laden turbulent suspension. I. Direct numerical simulations," J. Fluid Mech. **335**, 75–109 (1997).